

Research Article

Hydrothermal Synthesis of MoS₂/rGO Heterostructures for Photocatalytic Degradation of Rhodamine B under Visible Light

Thi Thuy Trang Phan,¹ Thi Thanh Huong Nguyen,¹ Ha Tran Huu,² Thanh Tam Truong,¹ Le Tuan Nguyen,¹ Van Thang Nguyen,^{1,2} Vy Anh Tran,^{3,4} Thi Lan Nguyen,¹ Hong Lien Nguyen,⁵ and Vien Vo^{1,2}

¹Faculty of Natural Sciences, Quy Nhon University, Quy Nhon 55000, Vietnam

²Applied Research Institute for Science and Technology, Quy Nhon University, Quy Nhon 55000, Vietnam

³Institute of Research and Development, Duy Tan University, Da Nang 50000, Vietnam

⁴Faculty of Environmental and Chemical Engineering, Duy Tan University, Da Nang 50000, Vietnam

⁵School of Chemical Engineering, Hanoi University of Science and Technology, Hanoi 100000, Vietnam

Correspondence should be addressed to Vien Vo; vovien@qnu.edu.vn

Received 30 March 2021; Accepted 26 June 2021; Published 29 July 2021

Academic Editor: Donglu Shi

Copyright © 2021 Thi Thuy Trang Phan et al. This is an open access article distributed under the Creative Commons Attribution License, which permits unrestricted use, distribution, and reproduction in any medium, provided the original work is properly cited.

MoS₂/rGO composites were synthesized by hydrothermal method from the precursors of MoS₂ and reduced graphene oxide (rGO) prepared in the former steps. The influence of the synthesis conditions including hydrothermal temperature and mass ratio of MoS₂ to rGO on the structure, morphology, and optical absorption capacity of the MoS₂/rGO composites was systematically investigated using physicochemical characterizations. The photocatalytic performance of as-prepared samples was investigated on the degradation of Rhodamine B under visible light, in which, the composites obtained at hydrothermal temperature of 180°C and MoS₂/rGO mass ratio of 4/1 exhibited the highest photodegradation efficiency of approx. 80% after 4 hours of reaction. This enhancement in photocatalytic behaviour of composites could be assigned to the positive effect of rGO in life time expansion of photoinduced electrons—holes.

1. Introduction

The limited source of fresh water in earth crust, which is suffering from pollution caused by the persistent organic pollutants such as dyes, pesticides, and antibiotics, raises a huge challenge for human being to find more sustainable way in use and recycling wastewater [1, 2]. A variety of strategies have been investigated in effort to remove those contaminants in wastewater for recycle or discard into environment within harmless effect [3, 4]. However, the traditional methods are tough to achieve high efficiency, owing to the sophisticated organic pollutants. The most prominent among applications is photocatalytic technology due to its advantageous features such as high light-harvesting efficiency, environmental safety, low cost, and thorough degradation using naturally available solar energy sources [5–7]. In recent years,

the transition metal oxide-based semiconductors, including TiO₂ and ZnO, have attracted much attention of scientific community by their promising photocatalytic performances [3, 8–10]. However, the nature as large band gap semiconductors limits their practical application due to the fact that they are only active under the UV light. Therefore, MoS₂ with narrow band gap and fully activated under visible light could overcome this limitation. Nevertheless, the high rate of recombination of photoinduced charge carriers in single-phase MoS₂ normally prohibits its photocatalytic performance. Therefore, the integration of two or more photocatalysts to form a composite has been favorably considered [11–18]. One of the most successful strategies in coupling materials toward a better photocatalytic performance is grafting with a highly electronic conductive counterpart such as carbon-based materials. Among this family of materials, graphene, a

two-dimensional (2D) material constructed from the sp^2 -hybridized carbon elements, has attracted interest owing to its unique properties such as large specific surface area, good electrical conductivity, and high optical transmittance [19, 20]. These properties allow graphene to be utilized in the broad scope of application, including adsorption, photocatalyst, supercapacitors, and batteries. It is considered as a potential support when combining with a semiconductor material, leading to reduction in the recombination rate of charge carriers [3]. Accordingly, semiconductor/graphene photocatalysts have been widely used in many areas, such as water splitting for H_2 evolution, CO_2 reduction, organic synthesis, disinfection, and advanced oxidation processes in wastewater treatment [21]. The chemical-exfoliated graphene oxide (GO) is reported as low electrical conductivity [22]. By the reduction of oxygen-based functional group on the surface, the reduced graphene oxide (rGO) with recover sp^2 -hybridized framework performs better electronic conduction [23]. Therefore, as an analogue of graphene, rGO is a promising candidate for coupling and improving the conductivity of final composite.

In this current work, we designed and highlighted the interfacial interaction of MoS_2 with rGO using a two-step hydrothermal process, in which rGO nanosheets functioned as a framework for scaffolding MoS_2 , leading to enhanced properties of MoS_2 /rGO hybrid nanostructures. Specifically, the impact of hydrothermal temperature and ratio of precursors has been systematically investigated. It was indicated by RhB degradation activities that the photocatalytic performance of the optimized MoS_2 /rGO conventional hybrid structure was substantially improved.

2. Materials and Methods

2.1. Chemicals. Chemicals used for this study include graphite powder ($\geq 99\%$), L-ascorbic acid ($\geq 99\%$), $KMnO_4$ ($\geq 99\%$), $NaNO_3$ ($\geq 99\%$), H_2SO_4 (98%), HCl (37%), H_2O_2 (30%), C_2H_5OH (98%), $(NH_4)_6Mo_7O_{24}\cdot 4H_2O$ ($\geq 99\%$), thiourea ($\geq 99\%$), and Rhodamin B ($\geq 99\%$), which were purchased from Merck and used as received without further purification.

2.2. Synthesis of Materials

2.2.1. Synthesis of Graphene Oxide. Graphene oxide (GO) was fabricated from graphite powder by the modified Hummer's method [24, 25]. Firstly, 15 mL of H_2SO_4 solution was slowly added to a 500 mL flask containing 0.6 g of graphite powder and 0.3 g of $NaNO_3$. The suspension was stirred for 24 hours at room temperature. Next, the mixture was cooled down to 3–5°C and kept at this temperature for 2 hours. Then, 1.8 g of $KMnO_4$ was added to the mixture and stirred for 5 hours at room temperature, which was then heated to 98°C, and kept at this temperature for 30 min. After that, the mixture was cooled down to 40°C in air. Thereafter, 90 mL distilled water and 7.5 mL H_2O_2 30% were added. Finally, the suspension was centrifuged, washed 3 times in diluted HCl (5%), 3 times in distilled water, 3 times in ethanol, and dried in air at 80°C for 12 hours. After that, ascorbic acid was employed as a reducing agent to achieve rGO.

2.2.2. Synthesis of MoS_2 /rGO Composites. Firstly, MoS_2 was synthesized via a facile method of annealing the mixture of $(NH_4)_6Mo_7O_{24}\cdot 4H_2O$ and $(NH_2)_2CS$ under Ar gas at 650°C as described in the previous publication [24]. The MoS_2 /rGO composites were fabricated from the two separate components (rGO and MoS_2) by the hydrothermal method. To investigate the influence of the hydrothermal temperature on the composite properties, a fixed weight ratio of MoS_2 to rGO (=4/1) was added to the ethanol-water solution before applying the ultrasonication for 1 h and continuously stirring for 5 h to form a homogeneous mixture. After that, the obtained mixture was transferred to a 100 mL Teflon-lined autoclave and heated at different temperatures (140, 160, 180, and 200°C) for 10 h. Finally, the obtained mixture was filtered, washed with water, and centrifuged before being dried at 80°C for 12 h to obtain the samples, which are denoted as MoS_2 /rGO (4/1- T) composites with $T = 140, 160, 180, \text{ and } 200^\circ\text{C}$, respectively. In order to investigate the effect of the ratio of MoS_2 to rGO, a series of samples with different weight MoS_2 /rGO ratios was prepared following the same procedure for MoS_2 /rGO (4/1-180°C) and denoted as MoS_2 /rGO (x -180°C) with $x = 2/1, 4/1, \text{ and } 6/1$, respectively.

2.3. Characterization of Materials. The crystal phase of the synthesized samples was characterized by the X-ray powder diffraction (Bruker D8 Advance with Ni-filtered Cu $K\alpha$ radiation ($\lambda = 1.5418 \text{ \AA}$)). The Fourier-transform infrared spectroscopy of the samples was recorded on FT-IR-GX-PerkinElmerLabRAM HR Evolution (Horiba) with a 647.1 nm laser as an excitation source. The surface morphology and elemental composition were analyzed by scanning electron microscope (SEM-SEM-JEOL-JSM 5410 LV) and energy scattering spectroscopy (EDX-JEOL 5410), respectively. The specific surface area obtained by Brunauer–Emmett–Teller (BET) analysis and pore size distribution from Barrett–Joyner–Halenda (BJH) technique were measured on a Tristar II 3202 instrument using N_2 adsorption-desorption at 77 K. The UV–Vis diffuse reflectance spectroscopy (UV-Vis-DRS) of the samples was analysed using UV-Vis-Cary 5000 spectrophotometer (Varian). The X-ray photoelectron spectroscopy (XPS) was recorded on Theta Probe AR-XPS System (Thermo Fisher Scientific). The Raman spectroscopy was carried out T64000 Raman with a 647.1 nm laser as an excitation source, and detector CCD was cooled by liquid nitrogen.

2.4. Evaluation of Photocatalytic Activity. The photocatalytic activities of the obtained materials were evaluated *via* the photodegradation of RhB in an aqueous solution under visible light irradiation. For a typical experiment, 100 mg of the catalyst was added into 400 mL of 20 mg/L RhB solution. Before illumination, the reaction mixture was stirred continuously for 2 h in the dark to reach adsorption-desorption equilibrium. Next, the mixture was illuminated by compact lamp (60 W–220 V). After every interval of 30 min, 4 mL of the reaction solution was collected and removed from the photocatalyst by centrifugation for further measurement. The residual concentration of RhB was recorded using a UV-Vis spectrometer.

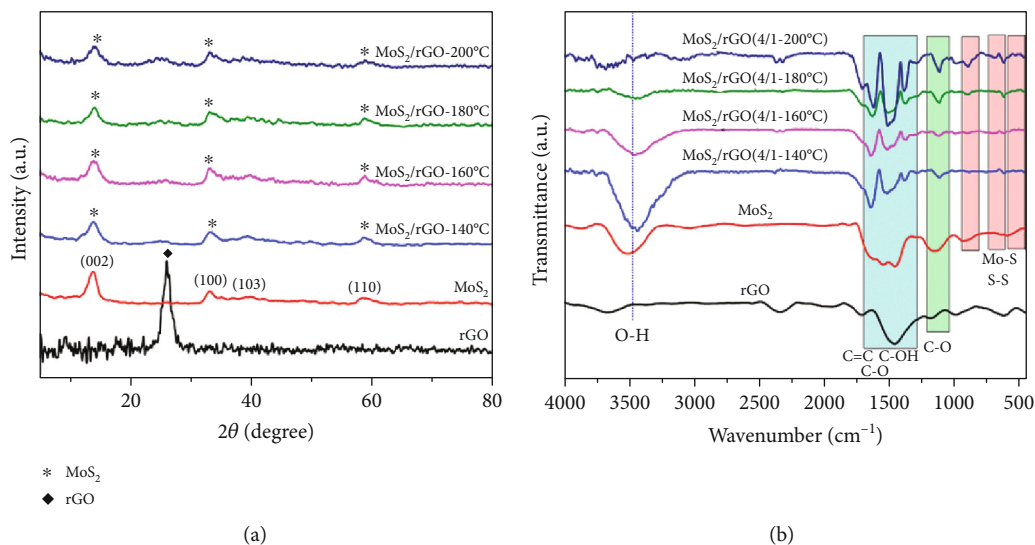


FIGURE 1: XRD patterns (a) and IR spectra (b) of rGO, MoS₂, and MoS₂/rGO (4/1-*T*) composites (*T* = 140, 160, 180, and 200°C).

3. Results and Discussion

3.1. Effect of the Hydrothermal Temperature. The effect of the hydrothermal temperature on the MoS₂/rGO composites was first investigated in a series of samples with a fixed weight ratio of MoS₂ to rGO (=4/1). The presence of MoS₂ in MoS₂/rGO (4/1-*T*) composites (*T* = 140, 160, 180, and 200°C) is confirmed by XRD and FT-IR showed in Figures 1(a) and 1(b), respectively.

According to Figure 1(a), the XRD patterns of MoS₂/rGO composites exhibit characteristic peaks at $2\theta = 14.1^\circ$; 33.6° ; 39.84° ; and 58.1° , which correspond to predominate (002), (100), (103), and (110) planes, respectively, and are consistent with the 2H hexagonal phase of MoS₂ [26]. These featured peaks in composites were obtuse and lower (peak at 002) than those of pristine MoS₂ due to the overlap of the rGO layers between MoS₂ crystals because of composite formation (as shown in Figure 1(a)). Notably, the intensity of the peaks corresponding to MoS₂ gradually decreases with the increase of temperature, indicating formation of a more solid and stable composite structure. A similar phenomenon was also observed in the previous report of Guo et al. [27].

To further evaluate the impact of MoS₂ supported on rGO nanosheet, chemical bonding characteristics of the as-prepared materials were revealed by the FTIR spectra (as shown in Figure 1(b)). While the peaks in the wavenumber of about 530, 630, and 920 cm⁻¹ can be assigned to Mo-S bonds [28–30], a peak at about 550 cm⁻¹ can be attributed S-S vibration modes [31]. The peaks in the range of 1550–1650 cm⁻¹ represent the bonds in *sp*² hybridization such as C=C and C-O-C [32]. Furthermore, a broad band from 1112 to 1393 cm⁻¹ is associated with the existence of C-O and C-OH bonds [33]. Vibration bands in the region of 3200–3700 cm⁻¹ can be ascribed to the -OH bonds from adsorbed H₂O molecules of the rGO in the composites. As the hydrothermal temperature increases, the intensity of most characteristic peaks decreases, especially at *T* = 180°C. At high temperature (*T* = 200°C), a reduction of functional

groups may come from change of rGO structure to almost-like grapheme [27].

UV-Vis-DRS curves of MoS₂ and MoS₂/rGO-*T* composites are presented in Figure 2(a). Accordingly, the absorption edges of both the MoS₂ and MoS₂/rGO composites extend to the wavelength range from 400 to 700 nm. Based on the absorption edge, the bandgap energy of as-synthesized composites obviously shift towards the visible light region, which proves that the combination of MoS₂ and rGO could enhance the light-harvesting ability and expand the optical absorption range to the region of solar energy [12]. As shown in Figure 2(b), the Tauc plots of MoS₂ and MoS₂/rGO-*T* composites were present using Kubelka–Munk equation:

$$(\alpha h\nu)^{1/n} = C(h\nu - E_g), \quad (1)$$

in which, $h\nu$ is incident photoenergy, C is constant, E_g is band gap value, and n is exponent. For direct band gap, $n = 1/2$ was applied, and the E_g value was determined as the intercept of tangent of Tauc plot on x -axis.

The SEM images for the MoS₂/rGO (4/1-*T*) composites are shown in Figure 3. It is obvious that the hydrothermal temperature exhibits a significant effect on the surface morphology of the MoS₂/rGO-*T* composites. For MoS₂/rGO (4/1-140°C) (Figure 3(a)), its morphology is in nanosheets, similar to rGO (Figure 3(e)), without the clear presence of the structure of MoS₂. When the hydrothermal temperature increases to 160°C, MoS₂ nanosheets in the form of flakes clearly appear on the material surface but nonuniformly distribute (Figure 3(b)). While at 180°C (Figure 3(c)), the composite displays uniform formation between MoS₂ layers and rGO nanosheets. However, as the hydrothermal temperature increases to 200°C (Figure 3(d)), the MoS₂ layers densely appeared, stacked, and covered the rGO nanosheets. This phenomenon is consistent with the results observed from the XRD patterns.

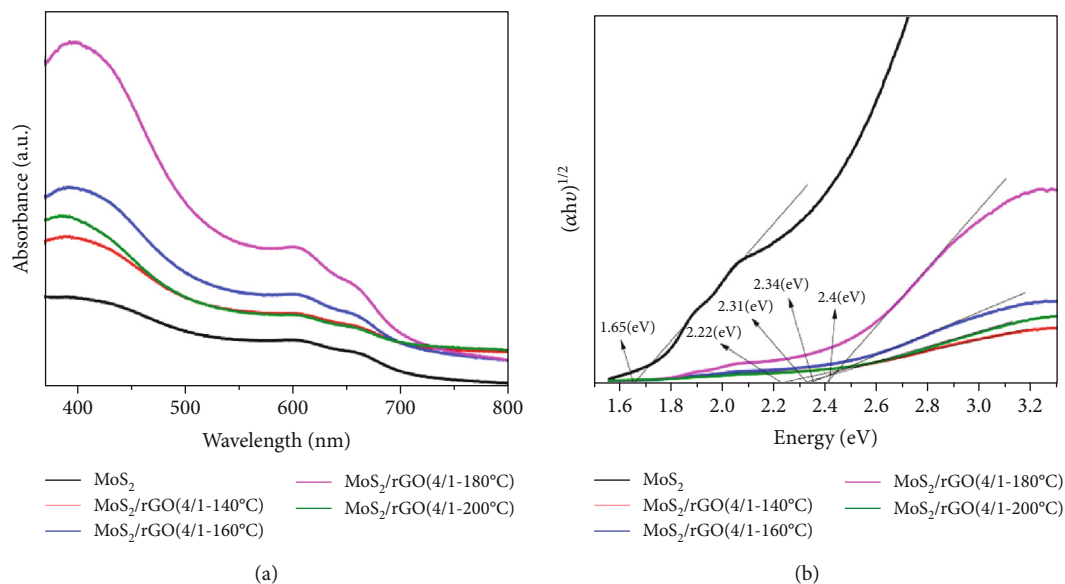


FIGURE 2: UV-Vis diffuse reflectance spectra of MoS_2 and MoS_2/rGO (4/1- T) composites ($T = 140, 160, 180,$ and 200°C).

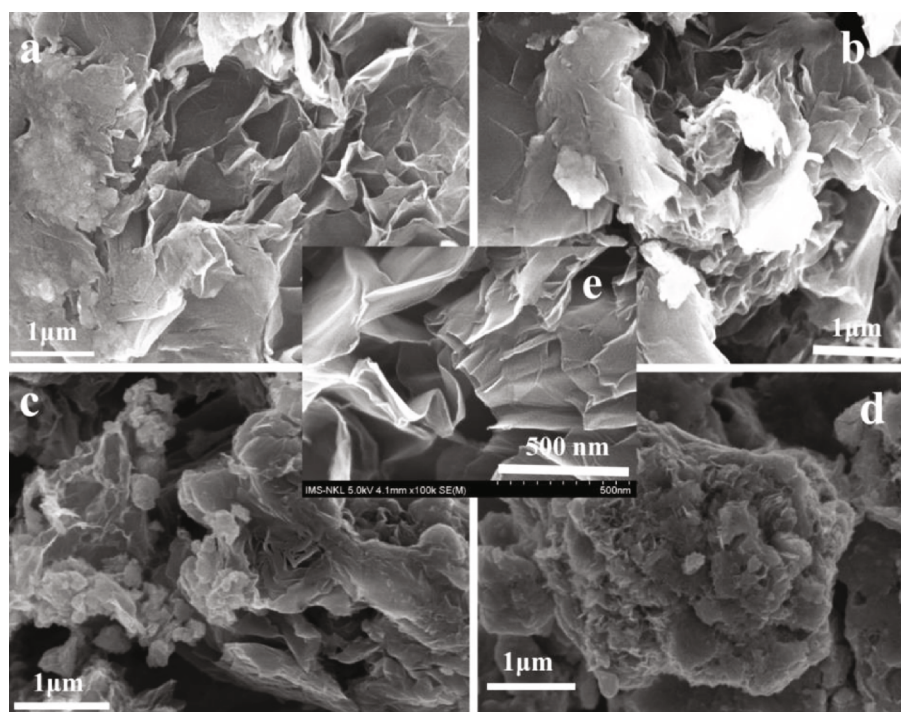


FIGURE 3: SEM images of MoS_2/rGO (4/1- 140°C) (a), MoS_2/rGO (4/1- 160°C) (b), MoS_2/rGO (4/1- 180°C) (c), MoS_2/rGO (4/1- 200°C) (d), and rGO (e).

The effect of the hydrothermal temperature on the photocatalytic activity of the MoS_2/rGO composites is shown in the photodegradation of RhB (Figure 4). For the single MoS_2 , the RhB decomposition efficiency is only 25.9% after 4 h under visible light irradiation. In contrast, the MoS_2/rGO composites exhibited higher catalytic activities and in the order MoS_2/rGO (4/1- 180°C) > MoS_2/rGO (4/1- 200°C) > MoS_2/rGO (4/1- 160°C) > MoS_2/rGO (4/1- 140°C), in

which decomposition efficiency for MoS_2/rGO (4/1- 180°C) reaches 80.0% (Figure 4(a)).

Additionally, in order to evaluate the kinetics of photocatalytic progress, the Langmuir-Hinshelwood model has been applied [34]. Figure 4(b) displays the linear relationship of $\ln(C_0/C)$ versus the irradiation time, indicating that the photodegradation of RhB fits well with the pseudo-first-order kinetic model according to the equation: $\ln(C_0/C) =$

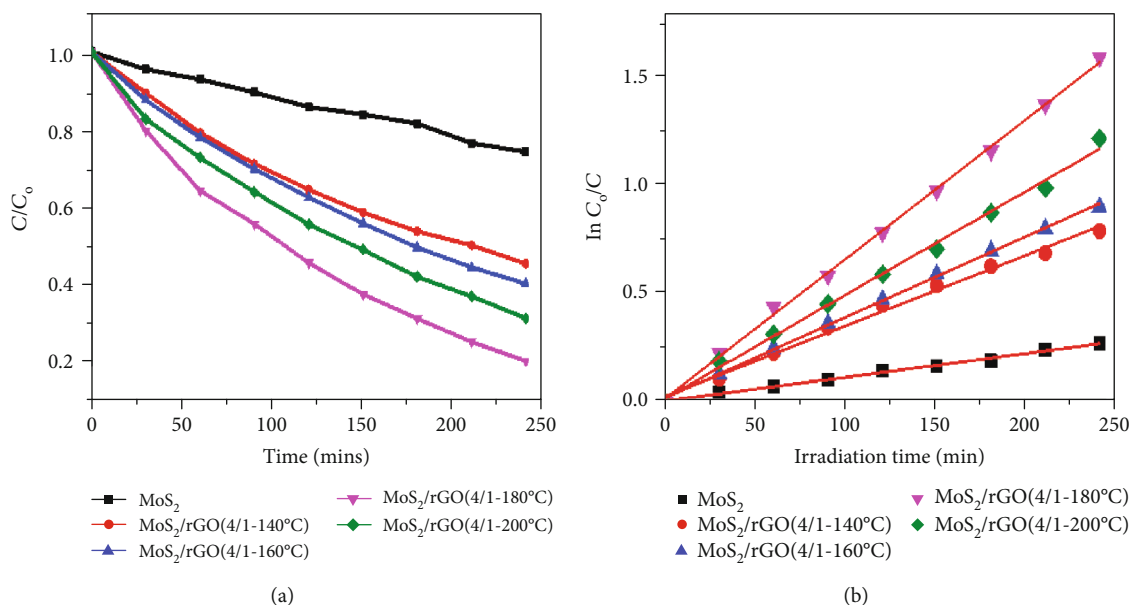


FIGURE 4: Effect of the hydrothermal temperature on the photocatalytic activity of the MoS_2/rGO composites in RhB decomposition (a) and their kinetic models (b).

TABLE 1: Rate constant of the photocatalytic degradation of RhB on the MoS_2/rGO composites at different hydrothermal temperatures.

Samples	MoS_2	MoS_2/rGO (4/1-140°C)	MoS_2/rGO (4/1-160°C)	MoS_2/rGO (4/1-180°C)	MoS_2/rGO (4/1-200°C)
Rate constant k_{app} (min^{-1})	0.00121	0.0033	0.00378	0.00652	0.00484
Correlation coefficients (R^2)	0.994	0.991	0.998	0.998	0.994

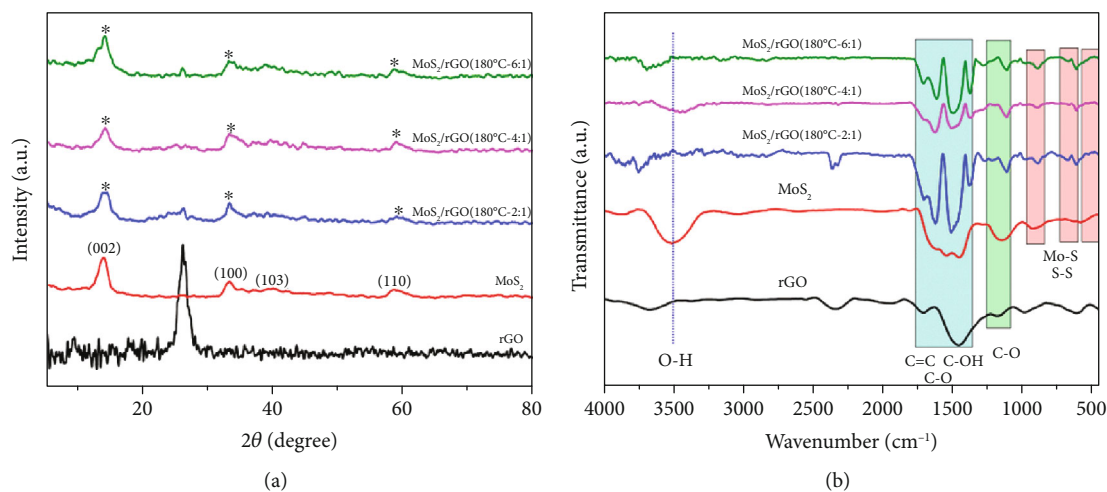


FIGURE 5: X-ray diffraction patterns (a) and IR spectra (b) of rGO, MoS_2 , and MoS_2/rGO (180°C- x) composites with $x = 2/1, 4/1,$ and $6/1$.

$k.t$, where C is the equilibrium concentration of RhB (mg/L), C_0 is the initial concentration of RhB before irradiation (mg/L), t is the reaction time (min), and k (min^{-1}) is the reaction rate constant. The obtained data are summarized in Table 1.

As observed in Table 1, MoS_2/rGO (4/1-180°C) performs the highest k value (0.00652 min^{-1}), which is about 5.3 times

higher than that of the pure MoS_2 . This observation is consistent with the above statement that MoS_2/rGO -180°C has more favourable hybrid structure and morphology as well as better light-harvesting ability than the remaining composites. Therefore, the hydrothermal condition of 180°C is considered to be the most appropriate, allowing the creation of more active MoS_2/rGO composites, reducing the

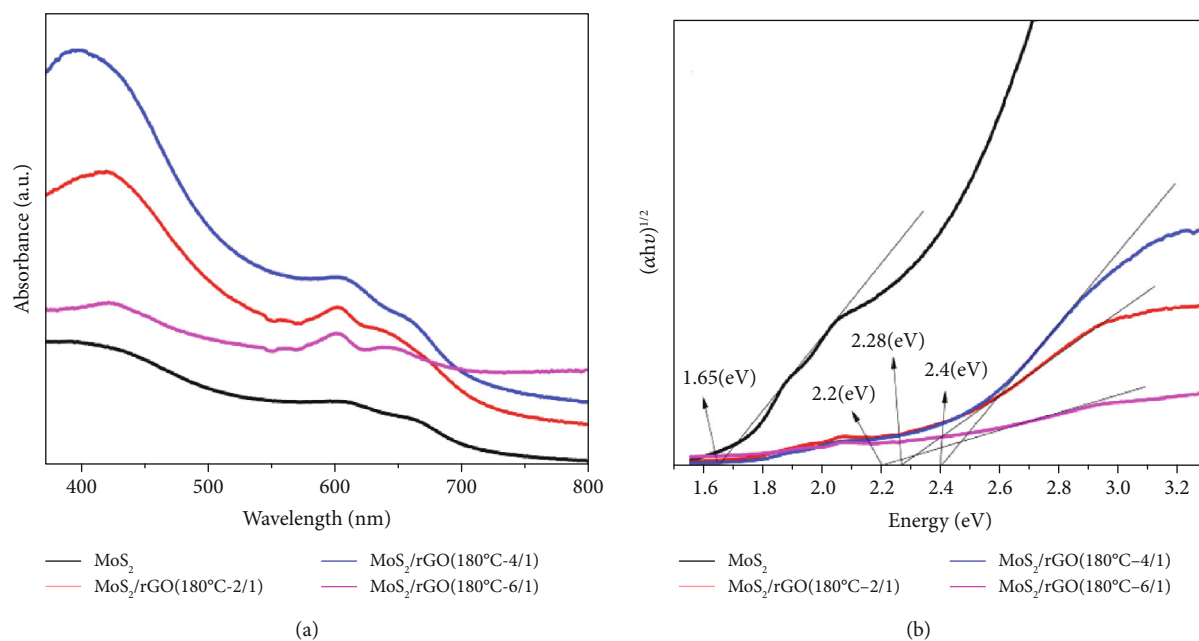


FIGURE 6: UV-Vis diffuse reflectance spectra of MoS_2 and MoS_2/rGO ($180^\circ\text{C}-x$) composites with $x = 2/1, 4/1$, and $6/1$.

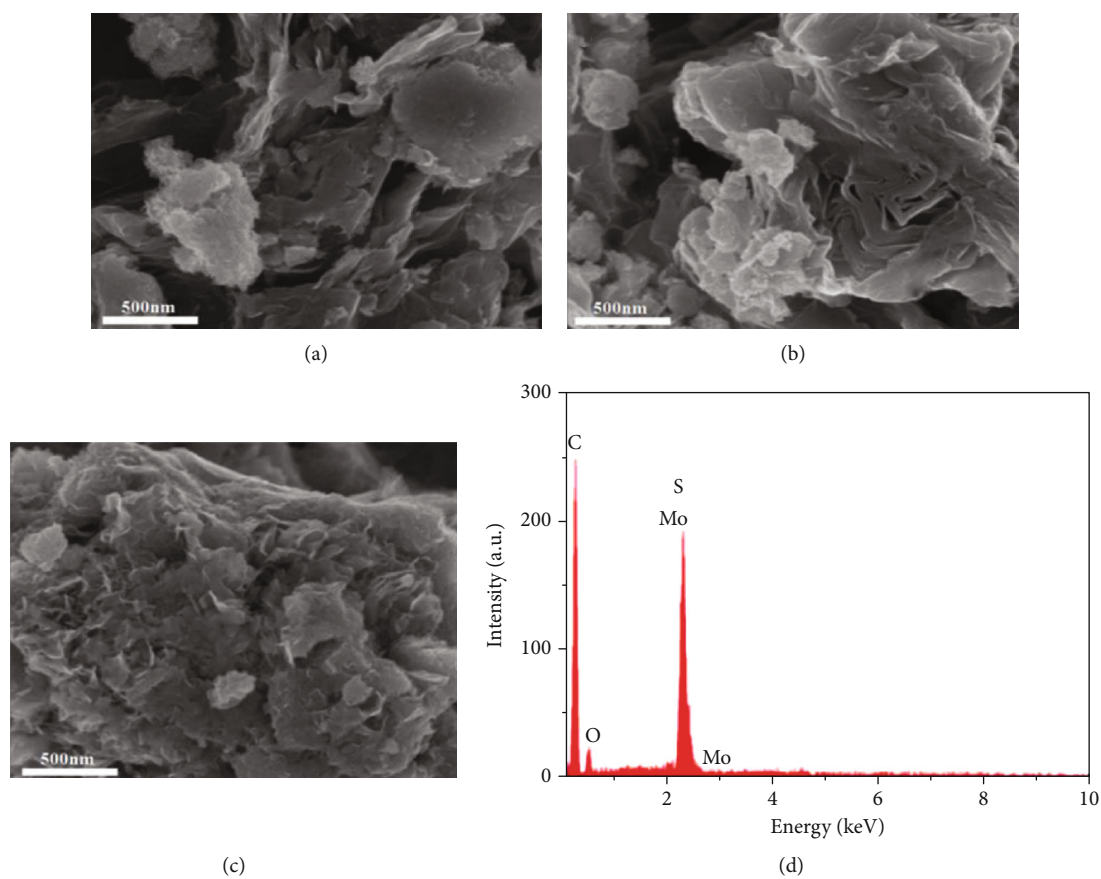


FIGURE 7: SEM images of MoS_2/rGO ($180^\circ\text{C}-x$) with $x = 2/1$ (a); $x = 4/1$ (b); $x = 6/1$ (c), and EDX of MoS_2/rGO ($180^\circ\text{C}-4/1$) (d).

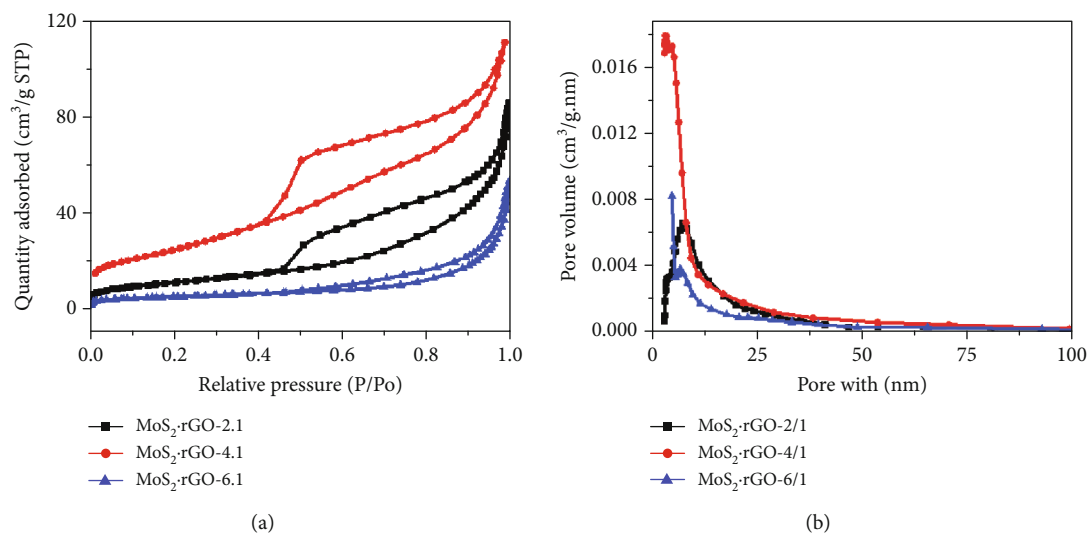


FIGURE 8: N₂ adsorption-desorption isotherms and pore-size distribution curves of MoS₂/rGO (180°C- x) with $x = 2/1, 4/1,$ and $6/1$.

TABLE 2: The characteristic parameters of MoS₂/rGO (180°C- x) with $x = 2/1, 4/1,$ and $6/1$ obtained from the BET method.

Parameter	MoS ₂ /rGO (180°C-2/1)	MoS ₂ /rGO (180°C-4/1)	MoS ₂ /rGO (180°C-6/1)
Specific surface area (m ² /g)	36.3	88.1	30.6
Total pore volume (cm ³ /g)	0.156802	0.174731	0.158113
Pore diameter (nm)	7.8–12.8	5.4–7.4	10.1–12.1

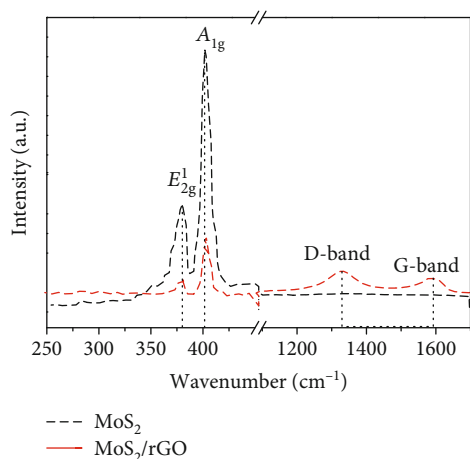


FIGURE 9: Raman spectra of MoS₂ and MoS₂/rGO (180°C-4/1).

recombination rate of photogenerated electron-hole pairs in the single MoS₂.

3.2. Effect of the Ratio of MoS₂ to rGO. Further investigation on the MoS₂ supported on rGO sheets substrate, the XRD patterns, and FT-IR spectra of selected samples with different mass MoS₂/rGO ratios are displayed in Figure 5.

As can be illustrated in Figure 5(a), the XRD patterns of the MoS₂/rGO composites exhibit characteristic peaks at $2\theta = 14.1; 33.6; 39.84; \text{ and } 58.1^\circ$ corresponding to the (002), (100), (103), and (110) planes, respectively, which are well

agreed with the 2H hexagonal phase of MoS₂ [26]. The increase of MoS₂/rGO mass ratio led to the gradually increase in intensity of MoS₂-related peaks, which could be clearly observed at the (002) lattice plane. Among the three composites, the pattern of the sample with ratio of 4/1 (MoS₂/rGO (4/1-180°C)) presents the most obtuse peak, indicating clear integration between graphene and MoS₂ nanosheets toward an uniform heterojunction.

The chemical bonding characteristics of the composites with various MoS₂/rGO ratios are displayed in Figure 5(b). The typical peaks of Mo-S, S-S, C-OH, CO, OH, and C=C functional groups at different wavenumbers (as mentioned in Section 3.1) all appeared in the composites. For MoS₂/rGO (4/1-180°C), however, the intensity of these peaks reduced significantly, suggesting a robust structure with intimate contact between the MoS₂ and rGO in the composite.

The optical absorption capacity of MoS₂ and the MoS₂/rGO composites was investigated by UV-Vis DRS. As shown in Figure 6(a), similar to the results obtained in changing the hydrothermal temperature, changes in the ratios of precursors lead to changes in the optical absorption intensity of the materials. Moreover, a dramatic shift in the absorption peak of the visible light region to around 700 nm appeared in all the composites. Moreover, the main peak systems of both MoS₂ and rGO present in these composites, which is consistent with previous reports [32]. This feature is favorable for increasing the light absorption ability as well as extending the optically active region of the composites to the low energy region (inherently abundant in the

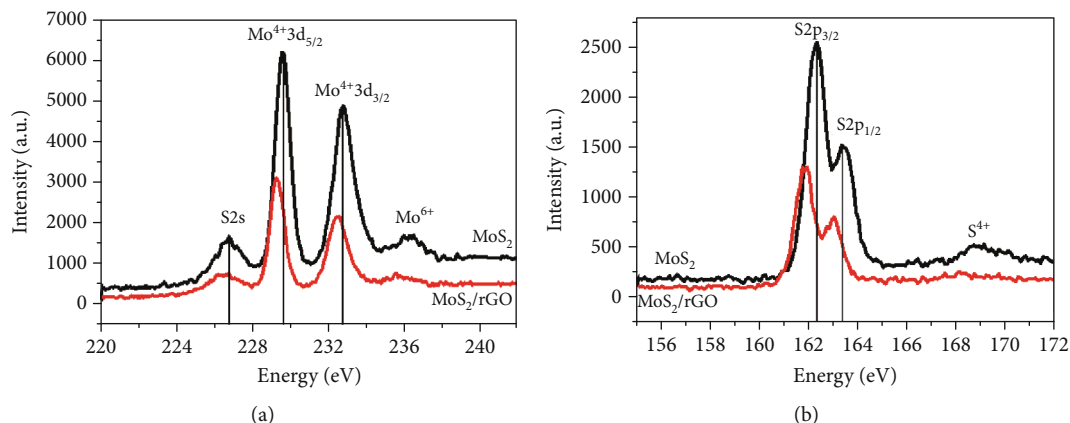


FIGURE 10: XPS spectra of Mo3d (a) and S2p (b) for MoS₂ and MoS₂/rGO (180°C-4/1).

sunlight region) (as shown in Figure 6(b)). Consequently, it is proved that the combination of intercalated MoS₂ nano-sheets and rGO layers plays an important role in increasing the photosensitivity of the materials.

The morphology of the materials with different ratios of MoS₂ is given in the SEM images. Figures 7(a)–7(c) display different surface structure morphology of the composites. Accordingly, the MoS₂ flakes appeared on rGO relatively little in MoS₂/rGO (2/1-180°C) (Figure 7(a)). Nevertheless, when increasing the ratio to 4/1 (Figure 7(b)), rGO was covered by a large number of MoS₂ flakes. With further increase in the ratio to 6/1 (Figure 7(c)), the layers of MoS₂ flakes appear more densely and tend to agglomerate together into large bulks. On the other hand, the EDX analysis of MoS₂/rGO (180°C-4/1) indicates that the atomic ratio of Mo to S is approximately 1 : 2, in accordance with the bonding properties of MoS₂ in the material structure (as shown in Figure 7(d)).

The specific surface area and porosity of the MoS₂/rGO (180°C-*x*) composites were confirmed by the BET analysis as illustrated in Figure 8. The hysteresis phenomenon and the hysteresis loops as shown in Figure 8(a) could be assigned to a type-IV isotherm (according to IUPAC classification), suggesting their mesoporous structure. The results in Table 2 show that the specific surface area of MoS₂/rGO-4/1 was higher than that of MoS₂/rGO-2/1 and MoS₂/rGO-6/1. This is in agreement with the aforementioned discussion of the SEM images, which may contribute to a significant enhancement in the photocatalytic efficiency of the material. The appropriate ratio of MoS₂ and rGO in MoS₂/rGO-2/1 and MoS₂/rGO-4/1 could provide a sufficient content of rGO framework assuring the better dispersion of MoS₂ nano-sheets. This leads to prevent components' nanosheets from recollapse then help enlarge their surface area. However, at higher content of MoS₂ (MoS₂/rGO-6/1), the insufficient rGO framework may cause the restacking of excess MoS₂. Therefore, the specific surface area of MoS₂/rGO-6/1 is the lowest value among three samples.

The Raman spectra of MoS₂ and a representative composite MoS₂/rGO (180°C-4/1) shown in Figure 9 exhibit two characteristic peaks located at wavenumbers of between 378 and 404 cm⁻¹, corresponding to the in-plane E_{2g}¹ and

out-of-plane A_{1g} vibration modes of the hexagonal phase of MoS₂ crystal [34]. An energy value difference between them corresponding to 26 cm⁻¹ reflects the multilayer structure of MoS₂ [35]. It is worth mentioning that the intensity of peaks at about 380 cm⁻¹ (internal vibration of Mo-S bond) and 405 cm⁻¹ (out-of-plane vibration of “S” element in Mo-S bond) of MoS₂/rGO (180°C-4/1) is much lower than that of the single MoS₂ that is suitable for the 2H-MoS₂ phase [36].

The intensity of the E_{2g}¹ peak is lower than that of the A_{1g} peak, indicating that the crystal structure of the obtained materials contains significant defect sites and side structures [23]. This observation is expected to enhance their photocatalytic activity. In addition, values at 1330 and 1590 cm⁻¹ can be related to D and G breathing vibrations, respectively, corresponding to the defects and sp² hybrid carbon atoms in the MoS₂/rGO composite [37]. This parameter indicates the presence of rGO integrated into MoS₂ to form a composite structure during the hydrothermal process. On the other hand, the I_D/I_G peak intensity ratio of 1.41 for MoS₂/rGO (180°C-4/1) is lower than that for rGO (I_D/I_G = 1.72), indicating a decrease in size and then density of the defect sites on the rGO surface in the composite compared to single rGO [23, 37].

To distinguish the existing forms of Mo and S in MoS₂ and MoS₂/rGO (4/1-180°C), X-ray photoelectron spectroscopy was performed. Figure 10(a) exhibits the binding energy values of S2s, Mo⁴⁺3d_{5/2}, Mo⁴⁺3d_{3/2}, and Mo⁶⁺ at photoelectron peaks of 226.7, 229.2, 232.5, and 235.5 eV, respectively [38]. In which the peaks of Mo⁴⁺3d_{5/2}, Mo⁴⁺3d_{3/2}, and S2s reflect the presence of the S-Mo-S bond in MoS₂. The binding energy of 235.5 eV corresponds to Mo⁶⁺ in the MoO₃ or MoO₄²⁻ compounds. The existence of this peak may come from the oxidation of Mo⁴⁺ to Mo⁶⁺ in the calcination process for preparing MoS₂. In addition, the results in Figure 10(b) show that the binding energy values at 161.9 and 163 eV can be assigned to S²⁻2p_{3/2} and S²⁻2p_{1/2} levels of the S²⁻ species in the composite [39]. All binding energy values at peaks of Mo3d and S2p in the composite shifted compared to that in single MoS₂ material, as described clearly in Figure 10. This shows that, in the hydrothermal process, there is an interaction of interlayer stacking between the

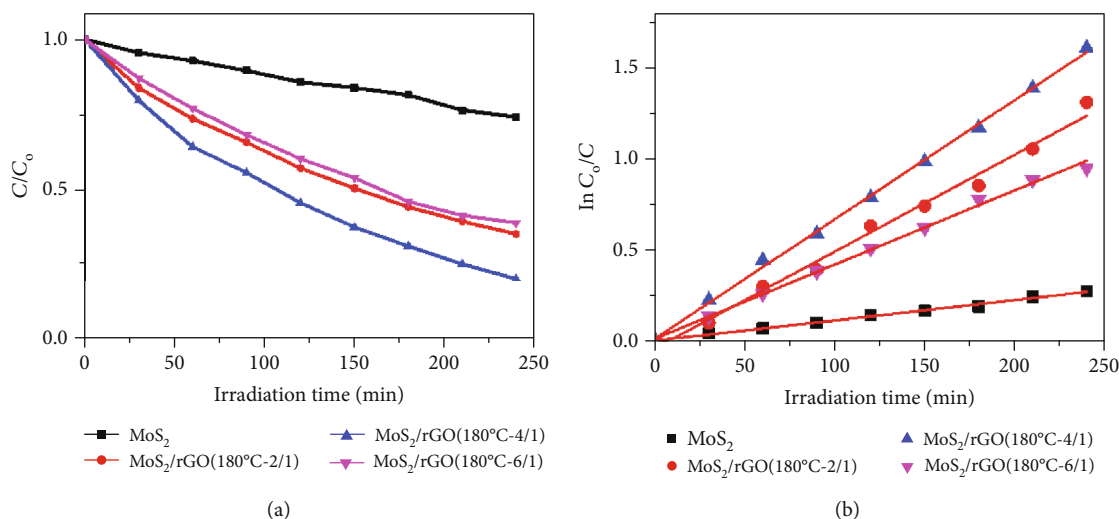


FIGURE 11: The change in C/C_0 (a) and $\ln C_0/C$ as a function of the irradiation time for MoS₂ and MoS₂/rGO composites under the illumination of the compact light (60 W–220 V).

TABLE 3: Kinetic data of MoS₂/rGO samples with different ratios.

Samples	MoS ₂	MoS ₂ /rGO (180°C-2/1)	MoS ₂ /rGO (180°C-4/1)	MoS ₂ /rGO (180°C-6/1)
Rate constant k_{app} (min ⁻¹)	0.00121	0.0053	0.00652	0.0041
Correlation coefficients (R^2)	0.994	0.988	0.998	0.995

MoS₂ layers on the rGO nanosheets in forming composites. Furthermore, the slight shift of Mo3d and S2p signal in the MoS₂/rGO composite to lower binding energy could be an evidence for the electrons transfer from MoS₂ to rGO which is expected to accelerate the separation of photoinduced electrons and holes.

These changes in the composite structure with different MoS₂/rGO ratios also have significant effects on the photocatalytic activity of the material in the degradation of MB (Figure 11). The results show that all the MoS₂/rGO composites exhibit a much higher catalytic activity compared to the sole component, MoS₂. Upon increasing the MoS₂ loading, the light absorption intensity of the composites increases, leading to boosting catalytic efficiency. Particularly, as the MoS₂/rGO ratio increased from 2/1 to 4/1, the degradation of RhB increased to approximately 80%. However, when this ratio increased to 6/1, photocatalytic degradation tended to decrease. This is attributed to that when the MoS₂ content overloads, it leads to aggregation on the surface of the rGO (as observed in the SEM image), which reduce the number of active sites and the light-harvesting ability in the visible region as well as the electron-hole transportation process. Therefore, the overloading of MoS₂ could limit the photocatalytic efficiency of the materials. Similar to the process of investigating the effects of temperature, the degradation of RhB in the composites with various ratios fits well with the pseudo-first-order kinetic model of Langmuir-Hinshelwood. The obtained data in Table 3 show that MoS₂/rGO (180°C-4/1) has a higher constant rate than the other samples. This can be explained by the synergistic effect between MoS₂ and

rGO, which enhanced the photocatalytic performance of the materials. Among the composites, MoS₂/rGO (180°C-4/1) displayed the most excellent efficiency of RhB degradation.

4. Conclusion

In this work, the MoS₂/rGO composites were synthesized *via* a hydrothermal method using MoS₂ and rGO as precursors. The impacts of hydrothermal temperature and mass ratio of MoS₂ to rGO on surface morphology, crystallographic phase, and optical property were investigated. The efficiency for RhB photodegradation of the optimal interfacially assembled MoS₂/rGO composites can reach approximately 80%, which is three times higher than that of the single component MoS₂. This observation is due to the reduction in electron-hole pair recombination and the enhancement in visible light harvesting. Therefore, this current work revealed that the optimized MoS₂/rGO composites could be a promising candidate for the photodegradation of persistent toxic organic compounds in aqueous solutions.

Data Availability

The data used to support the findings of this study are included within the article.

Conflicts of Interest

The authors declare that there are no conflicts of interest regarding the publication of this paper.

Acknowledgments

This work was financially supported by the Vietnam Ministry of Science and Technology (Grant no. NĐT.52.KR/19).

References

- [1] Q. T. H. Ta, E. Cho, A. Sreedhar, and J.-S. Noh, "Mixed-dimensional, three-level hierarchical nanostructures of silver and zinc oxide for fast photocatalytic degradation of multiple dyes," *Journal of Catalysis*, vol. 371, pp. 1–9, 2019.
- [2] H. Abu Hasan, M. H. Muhammad, and N. 'I. Ismail, "A review of biological drinking water treatment technologies for contaminants removal from polluted water resources," *Journal of Water Process Engineering*, vol. 33, article 101035, 2020.
- [3] Q. V. Thi, M. S. Tamboli, Q. Thanh Hoai Ta, G. B. Kolekar, and D. Sohn, "A nanostructured MOF/reduced graphene oxide hybrid for enhanced photocatalytic efficiency under solar light," *Materials Science and Engineering B*, vol. 261, article 114678, 2020.
- [4] A. Sreedhar, I. N. Reddy, Q. T. Hoai Ta, G. Namgung, E. Cho, and J.-S. Noh, "Facile growth of novel morphology correlated Ag/Co-doped ZnO nanowire/flake-like composites for superior photoelectrochemical water splitting activity," *Ceramics International*, vol. 45, no. 6, pp. 6985–6993, 2019.
- [5] M. N. Chong, B. Jin, C. W. K. Chow, and C. Saint, "Recent developments in photocatalytic water treatment technology: a review," *Water Research*, vol. 44, no. 10, pp. 2997–3027, 2010.
- [6] R. Ameta, S. Benjamin, A. Ameta, and S. C. Ameta, "Photocatalytic Degradation of Organic Pollutants: A Review," in *Materials Science Forum*, vol. 734, pp. 247–272, Trans Tech Publications Ltd, 2013.
- [7] D. N. Thoai, Q. T. Hoai Ta, T. T. Truong, H. van Nam, and G. van Vo, "Review on the recent development and applications of three dimensional (3D) photothermal materials for solar evaporators," *Journal of Cleaner Production*, vol. 293, article 126122, 2021.
- [8] Q. T. H. Ta, G. Namgung, and J.-S. Noh, "Facile synthesis of porous metal-doped ZnO/g-C₃N₄ composites for highly efficient photocatalysts," *Journal of Photochemistry and Photobiology A: Chemistry*, vol. 368, pp. 110–119, 2019.
- [9] A. Sreedhar, I. N. Reddy, Q. T. Hoai Ta, T. H. Phuon Doan, J. Shim, and J.-S. Noh, "Unveiling the impact of interfacially engineered selective V₂O₅ nanobelt bundles with flake-like ZnO and Co-ZnO thin films for multifunctional visible-light water splitting and toxic gas sensing," *Journal of Power Sources*, vol. 478, article 229081, 2020.
- [10] Z. Shayegan, C.-S. Lee, and F. Haghghat, "TiO₂ photocatalyst for removal of volatile organic compounds in gas phase - a review," *Chemical Engineering Journal*, vol. 334, pp. 2408–2439, 2018.
- [11] C. B. Roxlo, M. Daage, A. F. Ruppert, and R. R. Chianelli, "Optical absorption and catalytic activity of molybdenum sulfide edge surfaces," *Journal of Catalysis*, vol. 100, no. 1, pp. 176–184, 1986.
- [12] D. James and T. Zubkov, "Photocatalytic properties of free and oxide-supported MoS₂ and WS₂ nanoparticles synthesized without surfactants," *Journal of Photochemistry and Photobiology A: Chemistry*, vol. 262, pp. 45–51, 2013.
- [13] S. Li, Y. Li, L. Shao, and C. Wang, "Direct Z-scheme N-doped TiO₂/MoS₂ heterojunction photocatalyst for photodegradation of methylene blue under simulated sunlight," *Chemistry-Select*, vol. 6, no. 2, pp. 181–186, 2021.
- [14] Y. Fu, Z. Ren, J. Wu et al., "Direct Z-scheme heterojunction of ZnO/MoS₂ nanoarrays realized by flowing-induced piezoelectric field for enhanced sunlight photocatalytic performances," *Applied Catalysis B: Environmental*, vol. 285, article 119785, 2021.
- [15] Y. Chen, F. Su, H. Xie et al., "One-step construction of S-scheme heterojunctions of N-doped MoS₂ and S-doped g-C₃N₄ for enhanced photocatalytic hydrogen evolution," *Chemical Engineering Journal*, vol. 404, article 126498, 2021.
- [16] E.-J. Yu, H. C. Kim, H. J. Kim et al., "Anisotropic heteronano-crystals of Cu₂O-2D MoS₂ for efficient visible light driven photocatalysis," *Applied Surface Science*, vol. 538, article 148159, 2021.
- [17] L. Zhang, L. Sun, S. Liu, Y. Huang, K. Xu, and F. Ma, "Effective charge separation and enhanced photocatalytic activity by the heterointerface in MoS₂/reduced graphene oxide composites," *RSC Advances*, vol. 6, no. 65, pp. 60318–60326, 2016.
- [18] S. Min and G. Lu, "Sites for high efficient photocatalytic hydrogen evolution on a limited-layered MoS₂ cocatalyst confined on graphene sheets—the role of graphene," *Journal of Physical Chemistry C*, vol. 116, no. 48, pp. 25415–25424, 2012.
- [19] N. M. Julkapli and S. Bagheri, "Graphene supported heterogeneous catalysts: an overview," *International Journal of Hydrogen Energy*, vol. 40, no. 2, pp. 948–979, 2015.
- [20] R. R. Nair, P. Blake, A. N. Grigorenko et al., "Fine structure constant defines visual transparency of graphene," *Science*, vol. 320, no. 5881, p. 1308, 2008.
- [21] S. P. Lonkar and A. A. Abdala, "Applications of graphene in catalysis," *Journal of Thermodynamics & Catalysis*, vol. 5, article 100132, 2014.
- [22] S. Pei and H.-M. Cheng, "The reduction of graphene oxide," *Carbon*, vol. 50, no. 9, pp. 3210–3228, 2012.
- [23] D. B. Nimbalkar, H. H. Lo, P. V. R. K. Ramacharyulu, and S. C. Ke, "Improved photocatalytic activity of RGO/MoS₂ nanosheets decorated on TiO₂ nanoparticles," *RSC advances*, vol. 6, no. 38, pp. 31661–31667, 2016.
- [24] T. T. Trang Phan, T. T. Truong, H. T. Huu et al., "Visible light-driven Mn-MoS₂/rGO composite photocatalysts for the photocatalytic degradation of rhodamine B," *Journal of Chemistry*, vol. 2020, Article ID 6285484, 10 pages, 2020.
- [25] Q. T. H. Ta, G. Namgung, and J.-S. Noh, "Synthesis of Ag@rGO/gC₃N₄ layered structures and their application to toxic gas sensors: effect of Ag nanoparticles," *Electronic Materials Letters*, vol. 15, no. 6, pp. 750–759, 2019.
- [26] J. Prasad, A. K. Singh, K. K. Haldar, V. Gupta, and K. Singh, "Electromagnetic interference shielding effectiveness in 3D flower-like MoS₂-rGO/gadolinium-doped nanocomposites," *Journal of Alloys and Compounds*, vol. 788, pp. 861–872, 2019.
- [27] X. Guo, Y. Hou, R. Ren, and J. Chen, "Temperature-dependent crystallization of MoS₂ nanoflakes on graphene nanosheets for electrocatalysis," *Nanoscale Research Letters*, vol. 12, no. 1, article 2248, pp. 479–479, 2017.
- [28] D. Wang, X. Zhang, Y. Shen, and Z. Wu, "Ni-doped MoS₂ nanoparticles as highly active hydrogen evolution electrocatalysts," *RSC Advances*, vol. 6, no. 20, pp. 16656–16661, 2016.
- [29] C. Koventhan, V. Vinothkumar, S.-M. Chen et al., "Efficient hydrothermal synthesis of flake-like molybdenum disulfide

- for selective electrochemical detection of metal in water real samples,” *International Journal of Electrochemical Science*, vol. 15, pp. 7390–7406, 2020.
- [30] J. Wang, F. Sun, S. Yang et al., “Robust ferromagnetism in Mn-doped MoS₂ nanostructures,” *Applied Physics Letters*, vol. 109, no. 9, article 092401, 2016.
- [31] M. Murugan, M. R. Kumar, A. Alsalmeh, A. Alghamdi, and R. Jayavel, “Synthesis and property studies of molybdenum disulfide modified reduced graphene oxide (MoS₂-rGO) nanocomposites for supercapacitor applications,” *Journal of Nanoscience and Nanotechnology*, vol. 17, no. 8, pp. 5469–5474, 2017.
- [32] L. Zou, R. Qu, H. Gao et al., “MoS₂/RGO hybrids prepared by a hydrothermal route as a highly efficient catalytic for sonocatalytic degradation of methylene blue,” *Results in Physics*, vol. 14, article 102458, 2019.
- [33] Y. Du, J. Wang, Y. Zou et al., “Synthesis of molybdenum disulfide/reduced graphene oxide composites for effective removal of Pb(II) from aqueous solutions,” *Scientific Bulletin*, vol. 62, no. 13, pp. 913–922, 2017.
- [34] F. A. Aisien, N. A. Amenaghawon, and E. F. Ekpenisi, “Photocatalytic decolourisation of industrial wastewater from a soft drink company,” *Journal of Engineering and Applied Science*, vol. 9, pp. 11–16, 2013.
- [35] Y. Zhong, T. Shi, Y. Huang et al., “Three-dimensional MoS₂/graphene aerogel as binder-free electrode for Li-ion battery,” *Nanoscale Research Letters*, vol. 14, no. 1, article 2916, pp. 85–88, 2019.
- [36] Y. Zhou, G. Liu, X. Zhu, and Y. Guo, “Ultrasensitive NO₂ gas sensing based on rGO/MoS₂ nanocomposite film at low temperature,” *Sensors and Actuators B: Chemical*, vol. 251, pp. 280–290, 2017.
- [37] M. Choi, S. K. Koppala, D. Yoon, J. Hwang, S. M. Kim, and J. Kim, “A route to synthesis molybdenum disulfide-reduced graphene oxide (MoS₂-RGO) composites using supercritical methanol and their enhanced electrochemical performance for Li-ion batteries,” *Journal of Power Sources*, vol. 309, pp. 202–211, 2016.
- [38] W. Qin, T. Chen, L. Pan et al., “MoS₂-reduced graphene oxide composites via microwave assisted synthesis for sodium ion battery anode with improved capacity and cycling performance,” *Electrochimica Acta*, vol. 153, pp. 55–61, 2015.
- [39] N. Tronganh, Y. Yang, F. Chen et al., “SiO₂-assisted synthesis of layered MoS₂/reduced graphene oxide intercalation composites as high performance anode materials for Li-ion batteries,” *RSC Advances*, vol. 6, no. 78, pp. 74436–74444, 2016.